

Robust narrow-gap semiconducting behavior in square-net $\text{La}_3\text{Cd}_2\text{As}_6$

Mario M. Piva,^{1,2,3,*} Marein C. Rahn,^{1,4} Sean M. Thomas,¹ Brian L. Scott,¹ Pascoal G. Pagliuso,² Joe D. Thompson,¹ Leslie M. Schoop,⁵ Filip Ronning,¹ and Priscila F. S. Rosa¹

¹*Los Alamos National Laboratory, Los Alamos, New Mexico 87545, USA*

²*Instituto de Física “Gleb Wataghin”, UNICAMP, 13083-859, Campinas, SP, Brazil*

³*Max Planck Institute for Chemical Physics of Solids, Nöthnitzer Str. 40, D-01187 Dresden, Germany*

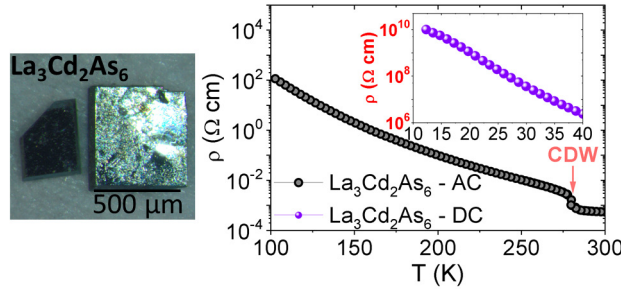
⁴*Institute for Solid State and Materials Physics,*

Technical University of Dresden, 01062 Dresden, Germany

⁵*Department of Chemistry, Princeton University, Princeton, NJ, 08544, USA*

(Dated: August 19, 2021)

ABSTRACT: Narrow-gap semiconductors are sought-after materials due to their potential for long-wavelength detectors, thermoelectrics, and more recently non-trivial topology. Here we report the synthesis and characterization of a new family of narrow-gap semiconductors, $R_3\text{Cd}_2\text{As}_6$ ($R = \text{La}, \text{Ce}$). Single crystal x-ray diffraction at room temperature reveals that the As square nets distort and Cd vacancies order in a monoclinic superstructure. A putative charge-density ordered state sets in at 279 K in $\text{La}_3\text{Cd}_2\text{As}_6$ and at 136 K in $\text{Ce}_3\text{Cd}_2\text{As}_6$ and is accompanied by a substantial increase in the electrical resistivity in both compounds. The resistivity of the La member increases by thirteen orders of magnitude on cooling, which points to a remarkably clean semiconducting ground state. Our results suggest that light square net materials within a $I4/mmm$ parent structure are promising clean narrow-gap semiconductors.



I. INTRODUCTION

Electronic instabilities are ubiquitous in quantum materials. Notable examples include spin-density waves, superconductivity, and charge-density waves (CDWs). The latter is a modulation of conduction electron density accompanied by a periodic distortion of the crystal lattice¹⁻³. Interestingly, CDWs have been recently observed in close proximity to exotic correlated phenomena, such as high-temperature superconductivity and axionic topological states⁴⁻⁷.

In addition, the formation of a CDW phase minimizes the energy of the system by opening a gap at the Fermi level, which may drive the material towards a narrow-gap semiconducting state¹⁻³. Disorder-free narrow-gap semiconducting materials are of interest due to their potential functionalities, which include thermoelectricity, dark-matter detection, and nontrivial topology⁸⁻¹⁰. Their narrow gap, however, often suffers from conducting in-gap states created by defects or impurities^{11,12}.

One way to design narrow-gap semiconductors is to search for low-dimensional crystal structures, which are

fundamentally unstable to the formation of energy gaps from small distortions¹⁻³. In fact, CDW phases were initially identified in one-dimensional (1D) transition metal trichalcogenides MX_3 ($M = \text{Nb}$ and Ta , $X = \text{S}, \text{Se}$, or Te) containing chains of NbSe_6 prisms and in quasi-2D layered transition metal dichalcogenides²⁻⁴.

Here we consider layered tetragonal materials with the “112” general formula RMX_2 ($R = \text{lanthanide}$, $M = \text{Au}, \text{Ag}, \text{Cu}, \text{Cd}$, and Zn , $X = \text{Bi}, \text{Sb}$, and As), which contain pnictide square nets. Previous band structure analysis and molecular orbital models have shown that square nets built from more electronegative elements are prone to distortions that lift the tetragonal symmetry¹³. This tendency occurs for two reasons. First, the R -square net p -bands close to the Fermi level (E_F) and the M d bands become well separated, which allows electron transfer and the formation of anionic units, that form covalent bonds leading to Zintl phases¹⁴⁻¹⁷. Second, there is greater mixing between s and p orbitals in pnictide elements with small atomic number (Z), which (again) favors the classic octet rule in a distorted structure over hypervalent bonds in an undistorted square net^{18,19}.

Important insights into distorted structures come from chalcogenide-based square nets, and numerous polytellurides host CDW phases with distorted Te square nets.

* Mario.Piva@cpfs.mpg.de

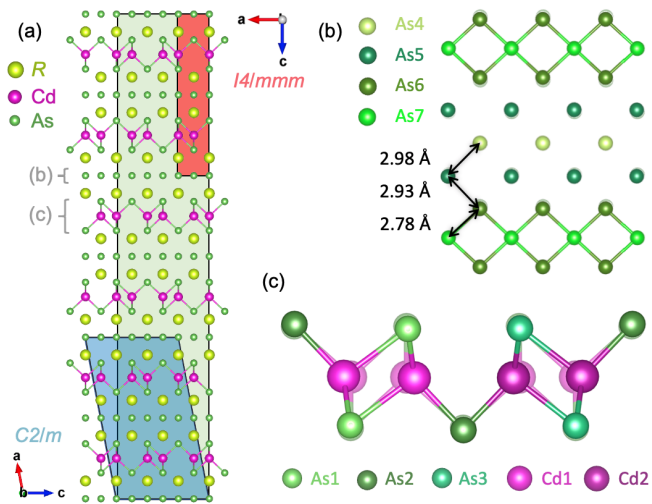


FIG. 1. (a) Structural relationship of the tetragonal CeCdAs_2 parent ($I4/mmm$, red), the conceptual orthorhombic $3 \times 1 \times 3$ vacancy superstructure (green) and the true, monoclinic, $\text{Ce}_3\text{Cd}_2\text{As}_6$ unit cell ($C2/m$, blue). (b) Detailed view of the As square-net layers. To emphasize the stripe distortion, only the short As6–As7 bonds are drawn. (c) Detailed view of the CdAs layers. For reference, the nominal undistorted structure is drawn as a shaded background. Cd ions are significantly displaced towards the vacancy stripes. As a consequence, the apical As ions As1 and As3 are slightly drawn towards the Cd layer, while the As2 ions dangling above/below the Cd-vacancy stripes are slightly pushed away from the Cd layer.

$RE\text{Te}_3$ ($RE = \text{rare-earth}$)^{20–22}, $\text{Pb}_{3-x}\text{Sb}_{1+x}\text{S}_4\text{Te}_{2-\delta}$ ²³, Sm_2Te_5 ²⁴, $\text{Cu}_{0.63}\text{EuTe}_2$ ²⁵, $AM\text{RTe}_4$ ($A = \text{K, Na and } M = \text{Cu, Ag}$)²⁶, and $\text{K}_{1/3}\text{Ba}_{2/3}\text{AgTe}_2$ ²⁷ are a few examples. In the latter, cation sites are partially occupied in order to satisfy the Zintl rule in the distorted structure. Importantly, the primary cause of the observed vacancy superstructure is argued to be a distortion in the tellurium square net, rather than the partial or complete ordering of the cations²⁷. Yet many distorted polytellurides exhibit metallic behavior^{25,26,28,29}. Recently, GdTe_3 has been shown to display a remarkably high electron mobility of $61,200 \text{ cm}^2\text{V}^{-1}\text{s}^{-1}$ at low temperatures³⁰. Ultra-high mobilities ($> 10,000 \text{ cm}^2\text{V}^{-1}\text{s}^{-1}$) and an anomalous Hall effect are also observed in pnictide square net materials such as EuMnBi_2 ³¹.

Here we highlight a route for clean narrow-gap semiconducting behavior in distorted arsenic square nets. We investigate a rather underexplored phase space in which $M = \text{post-transition metal}$ ^{32,33}. The substantial electronegativity of low- Z arsenic combined with the decrease in metallic character of post-transition metals provides a promising route to the realization of distortion-driven charge-density waves.

In this paper, we report the synthesis and characterization of distorted $\text{LaCd}_{2/3}\text{As}_2$ and $\text{CeCd}_{2/3}\text{As}_2$. At room temperature, both compounds crystallize in a vacancy superstructure of the $I4/mmm$ “112” parent structure and show semiconducting behavior. The ordered

superstructure thus corresponds to the “326” stoichiometry. As temperature is decreased, both compounds display a phase transition at $T_{\text{CDW}} = 136 \text{ K}$ and 278 K for $\text{Ce}_3\text{Cd}_2\text{As}_6$ and $\text{La}_3\text{Cd}_2\text{As}_6$, respectively. Given the many structural degrees of freedom due to the broken tetragonal symmetry, we attribute these transitions to CDW-driven structural distortions. This picture also explains the opening of a gap in the electronic density of states. Remarkably, the electrical resistivity of $\text{La}_3\text{Cd}_2\text{As}_6$ increases by thirteen orders of magnitude on cooling below T_{CDW} , in agreement with the vanishingly small Sommerfeld coefficient from specific heat measurements. The estimated activation energies from Arrhenius plots are $105(1) \text{ meV}$ and $74(1) \text{ meV}$ for $\text{La}_3\text{Cd}_2\text{As}_6$ and $\text{Ce}_3\text{Cd}_2\text{As}_6$, respectively.

II. EXPERIMENTAL DETAILS

Black plate-like single crystals of $\text{Ce}_3\text{Cd}_2\text{As}_6$ and $\text{La}_3\text{Cd}_2\text{As}_6$ were grown by the vapor transport technique. First, a polycrystalline seed of $1\text{La}:0.7\text{Cd}:2\text{As}$ was prepared via solid state reaction at $800 \text{ }^\circ\text{C}$. Then the polycrystalline powder was loaded along with iodine in a quartz tube, which was sealed in vacuum. The tube was kept in a temperature gradient from $830 \text{ }^\circ\text{C}$ to $720 \text{ }^\circ\text{C}$ for a week. The initial polycrystalline material was kept in the hot zone, and single crystals precipitated in the cold zone. The synthesized phase was investigated by $\text{Mo } K_\alpha$ single crystal x-ray diffraction and energy-dispersive x-ray spectroscopy (EDX) both at room temperature. EDX measurements confirmed the 3:2:6 stoichiometry within experimental error. The specific heat of a collection of approximately 10 single crystals (total mass $\approx 1 \text{ mg}$) was measured using a Quantum Design PPMS that employs a quasi-adiabatic thermal relaxation technique. The electrical resistivity (ρ) was characterized with the same instrument in the standard four-probe configuration. The current was applied in the basal plane of the crystal. For $\text{Ce}_3\text{Cd}_2\text{As}_6$, an AC bridge was used to measure ρ in all temperature range. While, for $\text{La}_3\text{Cd}_2\text{As}_6$, ρ was measured with an AC bridge, at high temperatures, whereas at low temperatures a DC method was required due to the large resistance of the sample.

III. RESULTS

We start with the structural characterization of $\text{Ce}_3\text{Cd}_2\text{As}_6$ and $\text{La}_3\text{Cd}_2\text{As}_6$. For both materials, Bragg reflections can be indexed in a tetragonal unit cell corresponding to the respective parent compounds with “112” stoichiometry. The approximate parameters of this $I4/mmm$ structure are given in Table I. The corresponding tetragonal cell is shaded red in Fig. 1(a). A detailed summary of the refined parameters of either compound is provided in the Supporting Information³⁴. The occupancy of the Cd site ($4d$ in $I4/mmm$) converges close

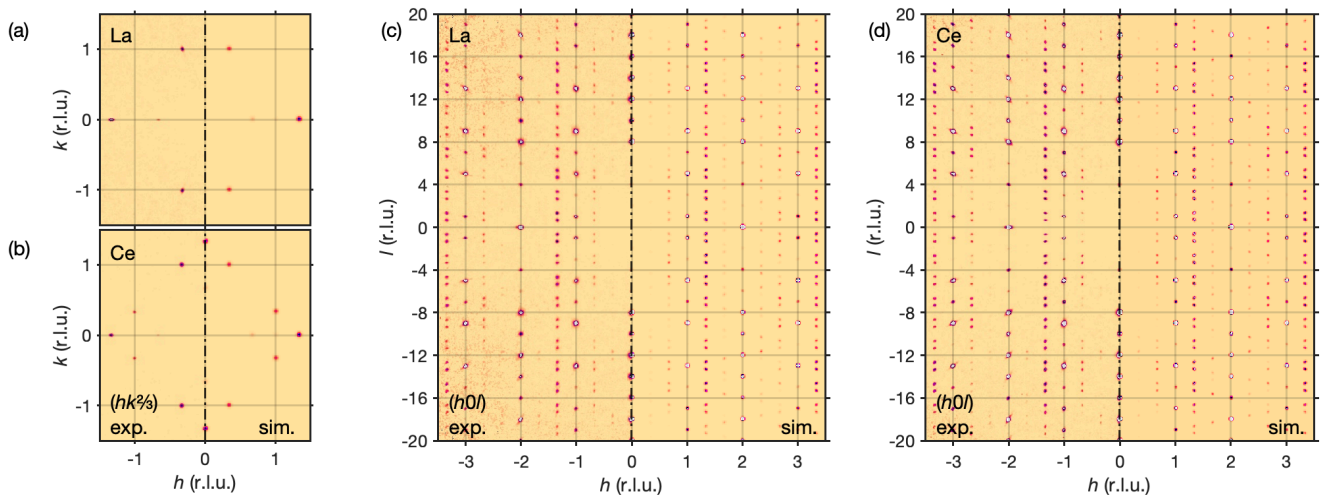


FIG. 2. Comparison of experimental and calculated x-ray diffraction intensity maps of reciprocal space. The left and right halves of each panel show the measured and calculated intensity, respectively. For convenience, the data is indexed in the $I4/mmm$ parent cell. (a,b) $(hk^2/3)$ slices reveal the presence of (a) two stripe domains (i.e., twins) in $\text{LaCd}_{0.67}\text{As}_2$ and (b) four in $\text{CeCd}_{0.67}\text{As}_2$. (c,d) $(h0l)$ slices show a large number of $q_{\text{Cd}} = \langle \frac{2}{3}0\frac{2}{3} \rangle$ superstructure peaks. The modulations of the intensities of these peaks is highly sensitive of small distortions of the ionic arrangement away from the nominal positions in the tetragonal parent.

to 66% in both materials, confirming the stoichiometry measured in EDX.

Interestingly, the Cd vacancies are not randomly distributed, but rather order in a stripe pattern. Fig. 2 shows x-ray intensity maps interpolated to the $(h, k, \frac{2}{3})$ and $(h0l)$ planes of reciprocal space (with reference to the $I4/mmm$ cell). Aside from the integer-index Bragg peaks, a pattern of weak satellite reflections is observed, which is described by the propagation vector $\mathbf{q}_{\text{Cd}} = \langle \frac{2}{3}, 0, \frac{2}{3} \rangle$. This indicates an ordering of the vacancies in a $3 \times 1 \times 3$ superstructure [green cell in 1(a)], which can be reduced to a base-centered monoclinic structure of space group $C2/m$ [blue cell in 1(a)].

Similar vacancy order has previously been observed in $\text{PrZn}_{0.67}\text{As}_2$ ($P4/nmm$). In that case, the vacancy pattern also results in a stoichiometric “326” compound, but with orthorhombic ($Pmnm$) symmetry³⁵. By contrast, the vacancy stripes in $\text{Ce}_3\text{Cd}_2\text{As}_6$ and $\text{La}_3\text{Cd}_2\text{As}_6$

$R\text{Cd}_{2/3}\text{As}_2$, $I4/mmm$ (#139), $Z = 4$
 $a_t = b_t \sim 4.1 \text{ \AA}$, $c_t \sim 21.3 \text{ \AA}$

ion, Wyck.	x	y	z	occ. (%)	
R	$4e$	0	0	0.11	100
Cd	$4d$	0	$1/2$	$1/4$	66
As1	$4c$	0	$1/2$	0	100
As2	$4e$	0	0	0.34	100

TABLE I. Structural parameters of $R_3\text{Cd}_2\text{As}_6$, inferred from refinements in a tetragonal cell (neglecting superstructure reflections). A detailed summary of refined parameters and uncertainties for either compound ($R = \text{La}, \text{Ce}$) is provided in the Supporting Information³⁴.

are staggered from one layer to the next in a sequence of six Cd layers. The transformation between the $I4/mmm$ and $C2/m$ cells, as illustrated in Fig. 2, is de-

$R_3\text{Cd}_2\text{As}_6$, $C2/m$ (#12, unique axis b , cell choice 1)

$$\begin{aligned} \vec{a} &= \vec{a}_t - \vec{c}_t, & \text{i.e. } a &= \sqrt{(a_t^2 + c_t^2)} \sim 21.6 \text{ \AA} \\ \vec{b} &= -\vec{b}_t, & \text{i.e. } b &= a_t \sim 4.1 \text{ \AA} \\ \vec{c} &= -3\vec{a}_t, & \text{i.e. } c &= 3a_t \sim 12.2 \text{ \AA} \\ \alpha &= \gamma = 90^\circ \\ \beta &= 90^\circ + \arctan(a_t/c_t) \sim 100.8^\circ \end{aligned}$$

ion	Wyck.	nominal position			deviation (\AA)	
		x	y	z	dx	dz
$R1$	$4i$	$z_{t,R}$	0	$z_{t,R}/3$		
$R2$	$4i$	$z_{t,R}$	0	$(z_{t,R} + 2)/3$		
$R3$	$4i$	$z_{t,R}$	0	$(z_{t,R} + 1)/3$		
Cd1	$4i$	$1/4$	0	$11/12$		-0.27
Cd2	$4i$	$1/4$	0	$7/12$		+0.23
As1	$4i$	$z_{t,As}$	0	$z_{t,As}/3$	-0.05	
As2	$4i$	$z_{t,As}$	0	$(z_{t,As} + 2)/3$	+0.11	
As3	$4i$	$z_{t,As}$	0	$(z_{t,As} + 1)/3$	-0.05	
As4	$2b$	0	$1/2$	0		
As5	$4i$	0	0	$1/6$		+0.13
As6	$4i$	$1/2$	0	$1/3$		+0.19
As7	$2c$	0	0	$1/2$		

TABLE II. Description of $R_3\text{Cd}_2\text{As}_6$ in the monoclinic setting. The parameters a_t , c_t , $z_{t,R} \sim 0.11$ and $z_{t,As} \sim 0.34$ refer to the $I4/mmm$ parent cells, as stated in Table I. All sites are fully occupied. The refined x and z coordinates of the Wyck-off site $4i$ for either compound are given in the Supporting Information³⁴. The right column states the resulting approximate deviation (in \AA) with respect to the nominal positions in the tetragonal parent cell.

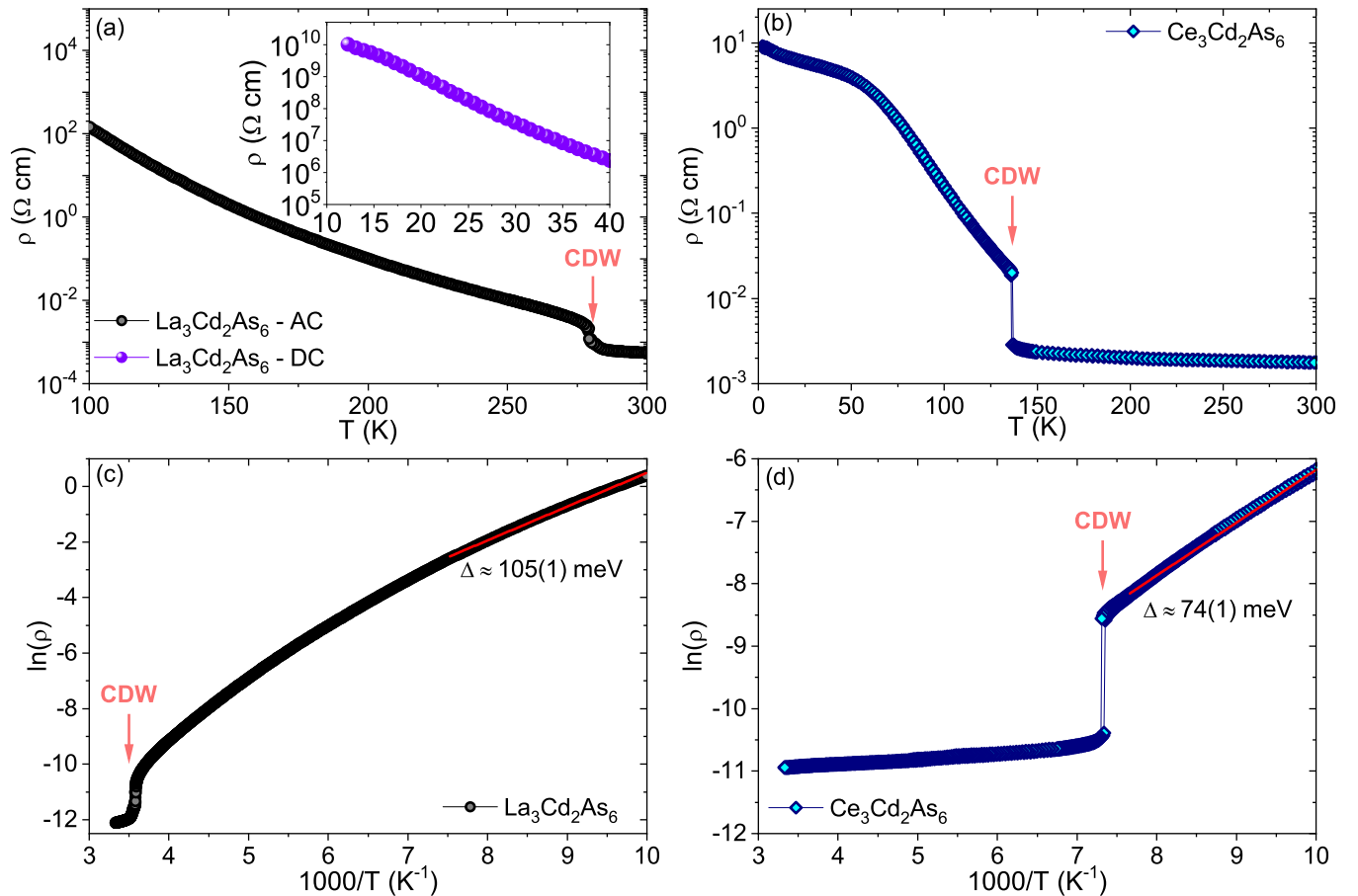


FIG. 3. (a) Electrical resistivity as a function of temperature for $\text{La}_3\text{Cd}_2\text{As}_6$. The inset shows the electrical resistivity of $\text{La}_3\text{Cd}_2\text{As}_6$ in the low temperature range. (b) Electrical resistivity as a function of temperature for $\text{Ce}_3\text{Cd}_2\text{As}_6$. Natural logarithm of the electrical resistivity as a function of 1000 over the temperature for $\text{La}_3\text{Cd}_2\text{As}_6$ (c) and for $\text{Ce}_3\text{Cd}_2\text{As}_6$ (d). The solid red lines are linear fits.

scribed in Table II. The resulting staircase of Cd-vacancy stripes breaks the parent compounds' fourfold symmetry, which is accompanied by several structural modifications. While the $I4/mmm$ parent structure is determined by two ionic position parameters, twenty are required to define the $C2/m$ counterpart (cf. Table II).

The satisfactory refinement within $I4/mmm$ when superstructure reflections are ignored shows that these distortions are weak. Nonetheless, small deviations of these parameters away from their value in the $I4/mmm$ setting cause significant variations of the structure factors of the superstructure peaks. This is illustrated in the reciprocal x-ray scattering intensity maps in Fig. 2. For comparison, each panel shows experimental intensities (left halves) along with our models (right halves). Details of this analysis are provided in the Supporting Information³⁴. Major ionic displacements are summarized in Table II in terms of the deviations (dx and dz) relative to the ionic positions in the tetragonal parent compound. The full summary of refined parameters and uncertainties is given in the Supporting Information³⁴.

The refinement adequately captures that the Bragg

intensities at $(\frac{2}{3}0l)$ are significantly weaker than those along $(\frac{4}{3}0l)$. This is due to a “relaxation” of Cd ions by about 0.25 \AA towards the vacancy stripes, as illustrated in Fig. 1(c). As expected, the displacement of Cd ions also leads to a measurable displacement of their ligands (As1, As2 and As3), which causes a characteristic modulation of superstructure intensities along the l direction in reciprocal space.

Importantly, the arsenic square nets in the new “326” structure are also distorted. Here, the high-symmetry As1 site of $I4/mmm$ splits into As4 – As7 (in $C2/m$). The As-As bond-lengths are then modulated by about 0.2 \AA , as illustrated in Fig. 1(b), and become shorter than hypervalent Sb-Sb distances. In the distorted case, the tolerance factor defined by $t = d_{\text{As-As}}/d_{\text{Ce/La-As}}$ is no longer valid^{18,19}. Whether the square-net distortion leads to Cd vacancies, similar to $\text{K}_{1/3}\text{Ba}_{2/3}\text{AgTe}_2$ in Ref. [22], or vice-versa remains an open question.

Finally, we note that no major structural differences have been observed between $\text{La}_3\text{Cd}_2\text{As}_6$ and $\text{Ce}_3\text{Cd}_2\text{As}_6$, aside from the expected lattice contraction from La to Ce, namely the volume of the Ce unit cell being smaller

by 2.1%. Nonetheless, the $\text{La}_3\text{Cd}_2\text{As}_6$ crystal investigated featured only two of the four expected crystallographic twins corresponding to four propagation directions of the vacancy staircase, as observed in $\text{Ce}_3\text{Cd}_2\text{As}_6$ [Figs. 2(a,b)]. This observation could stem from extrinsic reasons, such as finite strain during crystal growth.

We turn to the physical properties of $\text{La}_3\text{Cd}_2\text{As}_6$ single crystals. Figures 3(a) and (b) display the in-plane electrical resistivity (ρ) of $\text{La}_3\text{Cd}_2\text{As}_6$ and $\text{Ce}_3\text{Cd}_2\text{As}_6$, respectively. Upon cooling, a sudden increase in the resistivity is observed at $T_{\text{CDW}} = 279$ K for $\text{La}_3\text{Cd}_2\text{As}_6$ and at $T_{\text{CDW}} = 136$ K for $\text{Ce}_3\text{Cd}_2\text{As}_6$. Below T_{CDW} , the observed semiconducting behavior indicates the opening of an energy gap due to the CDW phase transition, similar to $\text{Sr}_3\text{Ir}_4\text{Sn}_{13}$, $\text{Ca}_3\text{Ir}_4\text{Sn}_{13}$ ³⁶, $\text{Ce}_3\text{Co}_4\text{Sn}_{13}$ and $\text{La}_3\text{Co}_4\text{Sn}_{13}$ ³⁷⁻⁴⁰. Notably, the resistivity of $\text{La}_3\text{Cd}_2\text{As}_6$ increases up to 10^{10} Ω cm at 12 K, as presented in the inset of Fig. 3(a). This large increase of thirteen orders in magnitude is a rare property in narrow-gap semiconductors, which are typically prone to impurity bands that may dominate the electronic properties at low temperatures^{11,12}. Remarkably, this increase was achieved in an as-grown single crystal, which suggests that sample quality could be improved through further purification. The broad hump around 50 K for $\text{Ce}_3\text{Cd}_2\text{As}_6$ may be associated with the depopulation of the first excited crystal-field state. The magnetic properties of $\text{Ce}_3\text{Cd}_2\text{As}_6$ will be the focus of a separate study.

Figures 3(c) and (d) present the resistivity in Ω m on a logarithmic scale, as a function of $(1000/T)$ for $\text{La}_3\text{Cd}_2\text{As}_6$ and $\text{Ce}_3\text{Cd}_2\text{As}_6$. An activated gap appears to open for temperatures below the CDW transition temperatures in both compounds. The activation energies can be estimated from linear fits, considering the Arrhenius equation $\ln(\rho_{xx}) = \ln(\rho_0) + \Delta/T$, yielding 105(1) meV and 74(1) meV for $\text{La}_3\text{Cd}_2\text{As}_6$ and $\text{Ce}_3\text{Cd}_2\text{As}_6$, respectively. We note that the gap values are an estimation and should be taken with caution. Further, it is clear from Fig. 3(c) that the gap value changes as a function of temperature. A temperature dependent activation energy may be caused by changes in the lattice parameters, due to thermal contraction, as observed in $\text{Ce}_3\text{Bi}_4\text{Pt}_3$ ⁴¹. Moreover, the presence of even small amounts of defects create extrinsic channels of conduction, such as variable range hopping and in-gap states^{11,12}, which can also be a sensible scenario for a temperature dependent gap. Optical measurements are needed to directly probe the semiconducting gap of $\text{La}_3\text{Cd}_2\text{As}_6$ and $\text{Ce}_3\text{Cd}_2\text{As}_6$.

Figure 4(a) displays the specific heat per mole of lanthanide divided by temperature (C_p/T) for both $\text{Ce}_3\text{Cd}_2\text{As}_6$ and $\text{La}_3\text{Cd}_2\text{As}_6$ as a function of temperature. The insets of Fig. 4(a) present a detailed view of the transition temperatures, which are characterized by peaks at 279 K and 136 K for $\text{La}_3\text{Cd}_2\text{As}_6$ and $\text{Ce}_3\text{Cd}_2\text{As}_6$, respectively, in agreement with the electrical resistivity measurements. At this temperature scale, the relevance of magnetic Ce correlations to this transition is unlikely.

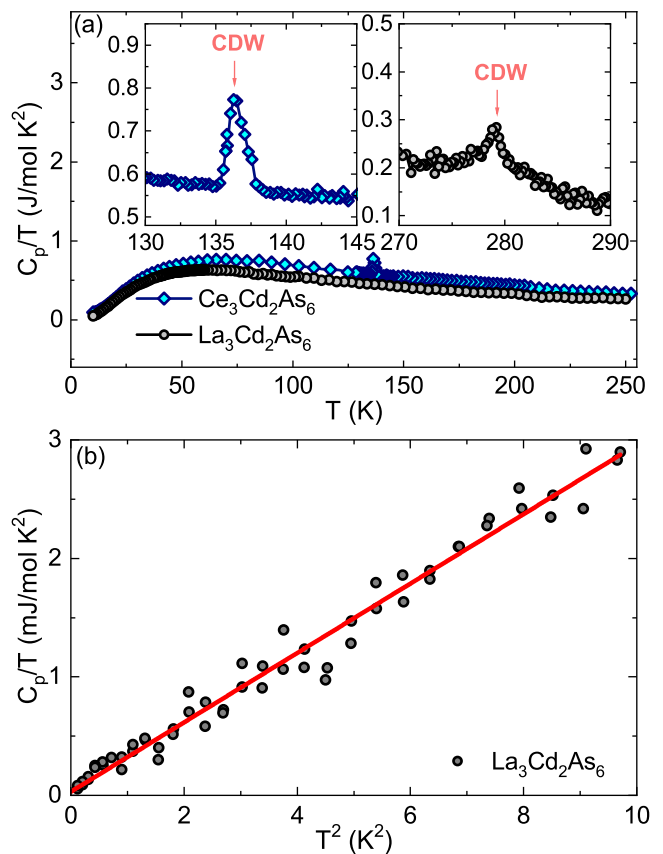


FIG. 4. (a) Specific heat over the temperature (C_p/T) as a function of temperature for $\text{Ce}_3\text{Cd}_2\text{As}_6$ and $\text{La}_3\text{Cd}_2\text{As}_6$. The insets show a zoom in view of the CDW phase transitions. (b) C_p/T as a function of T^2 for $\text{La}_3\text{Cd}_2\text{As}_6$. The solid red line is a linear fit.

Therefore, given the structural degree of freedom of As ions in the monoclinic structure, we attribute these transitions to a CDW phase caused by a further distortion in the arsenic square net. Figure 4(b) displays C_p/T per mole of lanthanide as a function of T^2 for $\text{La}_3\text{Cd}_2\text{As}_6$. The solid red line is the linear fit used to estimate the Sommerfeld coefficient (γ) of 0.03(3) mJ/molK² and a Debye temperature (θ_D) of 291(2) K for $\text{La}_3\text{Cd}_2\text{As}_6$. A negligible value of γ is expected in clean semiconducting compounds and confirms the high quality of $\text{La}_3\text{Cd}_2\text{As}_6$ single crystals.

The strong suppression of the CDW transition temperature and activation energy going from $\text{La}_3\text{Cd}_2\text{As}_6$ to $\text{Ce}_3\text{Cd}_2\text{As}_6$ is an indication that the application of external pressure may be an effective tuning parameter, given the volume unit cell contraction by about 2 % in $\text{Ce}_3\text{Cd}_2\text{As}_6$ as compared to $\text{La}_3\text{Cd}_2\text{As}_6$. High pressure experiments are needed to investigate whether the CDW phases in $\text{La}_3\text{Cd}_2\text{As}_6$ and $\text{Ce}_3\text{Cd}_2\text{As}_6$ can be suppressed, which may give rise to a superconducting state as in $\text{Sr}_3\text{Ir}_4\text{Sn}_{13}$, $\text{Ca}_3\text{Ir}_4\text{Sn}_{13}$ ³⁶ and $\text{La}_3\text{Co}_4\text{Sn}_{13}$ ⁴⁰. Moreover, chemical pressure may also be an effective tuning parameter, and hence single crystals with smaller lanthanide el-

ements, such as Pr or Nd, are desirable. Finally, spectroscopic experiments are necessary to search for electronic instabilities, which could be driving the CDW phase in $\text{La}_3\text{Cd}_2\text{As}_6$ and $\text{Ce}_3\text{Cd}_2\text{As}_6$.

IV. CONCLUSIONS

In summary, we report the structural and electrical transport properties of narrow-gap semiconductors $\text{Ce}_3\text{Cd}_2\text{As}_6$ and $\text{La}_3\text{Cd}_2\text{As}_6$, which crystallize in a distorted variant of the $I4/mmm$ tetragonal structure $RCd_{2/3}As_2$. The resulting base-centered monoclinic superstructure with $C2/m$ symmetry displays ordered Cd vacancies in a stripe pattern and a distorted As square net. Notably, both compounds feature charge density wave phases below 136 K ($\text{Ce}_3\text{Cd}_2\text{As}_6$) and 279 K ($\text{La}_3\text{Cd}_2\text{As}_6$), which suggests further distortion in the As square net. The CDW phases in these materials create gaps with estimated values of 105(1) meV and 74(1) meV for $\text{La}_3\text{Cd}_2\text{As}_6$ and $\text{Ce}_3\text{Cd}_2\text{As}_6$. A remarkable increase of thirteen orders of magnitude in the electrical resistivity was found for $\text{La}_3\text{Cd}_2\text{As}_6$ upon cooling from room temperature to 12 K. Coupled to the vanishingly small specific heat Sommerfeld coefficient, this result not only points to a robust semiconducting ground state in this class of compounds but also provides a route to realize clean narrow-gap semiconductors in distorted arsenic square net materials.

V. SUPPORTING INFORMATION

The Supporting Information consists of tables summarizing the crystallographic structure data for $\text{La}_3\text{Cd}_2\text{As}_6$

and $\text{Ce}_3\text{Cd}_2\text{As}_6$ and the complete crystallographic information files for both compounds at room temperature.

ACKNOWLEDGMENTS

We acknowledge useful discussions with Peter Abbamonte. Work at Los Alamos was performed under the auspices of the U.S. Department of Energy, Office of Basic Energy Sciences, Division of Materials Science and Engineering under project ‘‘Quantum Fluctuations in Narrow-Band Systems’’. This work was also supported by the Sao Paulo Research Foundation (FAPESP) grants 2015/15665-3, 2017/10581-1, 2017/25269-3, CNPq grant # 304496/2017-0 and CAPES, Brazil. Scanning electron microscope and energy dispersive X-ray measurements were performed at the Center for Integrated Nanotechnologies, an Office of Science User Facility operated for the U.S. Department of Energy (DOE) Office of Science. This research has been supported by the Deutsche Forschungsgemeinschaft through the SFB 1143 and the Wurzburg-Dresden Cluster of Excellence EXC 2147 (ct.qmat). Work at Princeton was supported by the Arnold and Mabel Beckman Foundation through a Beckman Young Investigator grant awarded to L.M.S.

REFERENCES

- [1] Monceau, P. Electronic crystals: an experimental overview. *Adv. Phys.* **61** 325 (2012).
- [2] Gruner, G. The dynamics of charge-density waves. *Rev. Mod. Phys.* **60**, 1129 (1988).
- [3] Wilson, J. A.; Di Salvo, F. J.; Mahajan, S. Charge-density waves and superlattices in the metallic layered transition metal dichalcogenides. *Advances in Physics* **24:2** 117-201 (1975).
- [4] Chen, C.-W.; Choe, J.; Morosan, E. Charge density waves in strongly correlated electron systems. *Rep. Prog. Phys.* **79** 084505.
- [5] Loret, B.; Auvray, N.; Gallais, Y.; Cazayous, M.; Forget, A.; Colson, D.; Julien, M.-H.; Paul, I.; Civelli, M.; Sacuto, A.; Intimate link between charge density wave, pseudogap and superconducting energy scales in cuprates. *Nat. Phys.* **15** 771-775 (2019).
- [6] Gooth, J.; Bradlyn, B.; Honnali, S.; Schindler, C.; Kumar, N.; Noky, J.; Qi, Y.; Shekhar, C.; Sun, Y.; Wang, Z.; Bernevig, B. A.; Felser, C. Axionic charge-density wave in the Weyl semimetal $(\text{TaSe}_4)_2\text{I}$. *Nature* **575** 315-319 (2019).
- [7] Shi, W.; Wieder, B. J.; Meyerheim, H. L.; Sun, Y.; Zhang, Y.; Li, Y.; Shen, L.; Qi, Y.; Yang, L.; Jena, J.; Werner, P.; Koepf, K.; Parkin, S.; Chen, Y.; Felser, C.; Bernevig, B. A.; Wang, Z. A charge-density-wave topological semimetal. *Nature Phys.* 1745-2481 (2021).
- [8] Tomczak, J. M. Thermoelectricity in correlated narrow-gap semiconductors. *J. Phys.: Condens. Matter* **30** 183001 (2018).
- [9] Hochberg, Y.; Kahn, Y.; Lisanti, M.; Zurek, K. M.; Grushin, A. G.; Ilan, R.; Griffin, S. M.; Liu, Z.-F.; Weber, S. F.; Neaton, J. B. Detection of sub-MeV dark matter with three-dimensional Dirac materials. *Physical Review D* **97** 015004 (2018).
- [10] Xiao, Y.; Wang, D.; Qin, B.; Wang, J.; Wang, G.; Zhao, L.-D. Approaching Topological Insulating States Leads to High Thermoelectric Performance in n-Type PbTe. *J. Am. Chem. Soc.* **140** 13097-13102 (2018).
- [11] Shklovskii, Boris I.; Efros, Alex L. *Electronic Properties of Doped Semiconductors*; 1st Edition, Springer, Berlin,

- 1984, pp. 74-82.
- [12] Seeger, Karlheinz. *Semiconductor Physics - An Introduction*; 9th Edition, Springer, Vienna, 2004, pp. 5-9.
- [13] Tremel, W.; Hoffmann, R. Square nets of main-group elements in solid-state materials. *J. Am. Chem. Soc.* **109** 124-140 (1987).
- [14] Zintl, E.; Dullenkopf, W. Polyantimonide, Polywismutide und ihr Übergang in Legierungen. *Z. Phys. Chem.* **B16** 183-194 (1932).
- [15] Zintl, E.; Dullenkopf, W. Intermetallische Verbindungen. *Angew. Chem.* **52** 133-142 (1939).
- [16] Ovchinnikov, A.; Bobev, S. Zintl phases with group 15 elements and the transition metals: A brief overview of pnictides with diverse and complex structures. *J. Solid State Chem.* **270** 346-359 (2019).
- [17] Rosa, P.; Xu, Y.; Rahn, M.; Souza, J.; Kushwaha, S.; Veiga, L.; Bombardi, A.; Thomas, S.; Janoschek, M.; Bauer, E.; Chan, M.; Wang, Z.; Thompson, J.; Harrison, N.; Pagliuso, P.; Bernevig, A.; Ronning, F. Colossal magnetoresistance in a nonsymmorphic antiferromagnetic insulator. *npj Quantum Mater.* **5** 52 (2020).
- [18] Klemenz, S.; Hay, A. K.; Teicher, S. M. L.; Topp, A.; Cano, J.; Schoop, L. M. The Role of Delocalized Chemical Bonding in Square-Net-Based Topological Semimetals. *J. Am. Chem. Soc.* **142** (13) 6350-6359 (2020).
- [19] Papoian, G. A.; Hoffmann, R. Hypervalent Bonding in One, Two, and Three Dimensions: Extending the Zintl-Klemm Concept to Nonclassical Electron-Rich Networks. *Angew. Chem., Int. Ed.* **2000**, 39, 2408-2448.
- [20] Malliakas, C.; Billinge, S. J. L.; Kim, H. J.; Kanatzidis, M. G. Square Nets of Tellurium: Rare-Earth Dependent Variation in the Charge-Density Wave of $RETe_3$ ($RE = \text{Rare-Earth Element}$). *J. Am. Chem. Soc.* **127** 6510 (2005).
- [21] Gweon, G.-H.; Denlinger, J. D.; Clack, J. A.; Allen, J. W.; Olson, C. G.; DiMasi, E. D.; Aronson, M. C.; Foran, B.; Lee, S. Direct Observation of Complete Fermi Surface, Imperfect Nesting, and Gap Anisotropy in the High-Temperature Incommensurate Charge-Density-Wave Compound $SmTe_3$. *Phys. Rev. Lett.* **81** 886 (1998).
- [22] Brouet, V.; Yang, M. L.; Zhou, X. J.; Hussain, Z.; Ru, N.; Shin, K. Y.; Fisher, I. R.; Shen, Z. X. Fermi Surface Reconstruction in the CDW State of $CeTe_3$ Observed by Photoemission. *Phys. Rev. Lett.* **93** 126405 (2004).
- [23] Chen, H.; Malliakas, C. D.; Narayan, A.; Fang, L.; Chung, D. Y.; Wagner, L. K.; Kwok, W.-K.; Kanatzidis, M. G. Charge Density Wave and Narrow Energy Gap at Room Temperature in 2D $Pb_{3-x}Sb_{1+x}S_4Te_{2-\delta}$ with Square Te Sheets. *J. Am. Chem. Soc.* **139** 32 (2017).
- [24] Malliakas, C. D.; Iavarone, M.; Fedor, J.; Kanatzidis, M. G. Coexistence and Coupling of Two Distinct Charge Density Waves in Sm_2Te_5 . *J. Am. Chem. Soc.* **130** 3310 (2008).
- [25] Malliakas, C. D.; Kanatzidis, M. G. A Double Charge Density Wave in the Single Tellurium Square Net in $Cu_{0.63}EuTe_2$? *J. Am. Chem. Soc.* **131** 20 (2009).
- [26] Malliakas, C. D.; Kanatzidis, M. G. Charge Density Waves in the Square Nets of Tellurium of $AMRETe_4$ ($A = K, Na; M = Cu, Ag; RE = La, Ce$). *J. Am. Chem. Soc.* **129** 35 (2007).
- [27] Zhang, X.; Li, J.; Foran, B.; Lee, S.; Guo, H.-Y.; Hogan, T.; Kannevurf, C. R.; Kanatzidis, M. G. Distorted Square Nets of Tellurium in the Novel Quaternary Polytelluride $K_{0.33}Ba_{0.67}AgTe_2$. *J. Am. Chem. Soc.* **117** 10513 (1995).
- [28] Iyeiri Y.; Okumura, T.; Michioka, C.; Suzuki, K.; Magnetic properties of rare-earth metal tritellurides RTe_3 ($R = Ce, Pr, Nd, Gd, Dy$). *Phys. Rev. B* **67** 144417 (2003).
- [29] DiMasi, E.; Foran, B.; Aronson, M. C.; Lee, S. Quasi-two-dimensional metallic character of Sm_2Te_5 and $SmTe_3$. *Chem. Mater.* **6** 1867-1874 (1994).
- [30] Klemenz, S.; Gao, T.; Rodolakis, F.; McChesney, J. L.; Ast, C. R.; Yazdani, A.; Burch, K. S.; Wu, S.; Ong, N. P.; Schoop, L. M. High mobility in a van der Waals layered antiferromagnetic metal. *Sci. Adv.* **6** eaay6407 (2020).
- [31] Masuda, H.; Sakai, H.; Tokunaga, M.; Yamasaki, Y.; Miyake, A.; Shiogai, J.; Nakamura, S.; Awaji, S.; Tsukazaki, A.; Nakao, H.; Murakami, Y.; Arima, T.; Tokura, Y.; Ishiwata, S.; Quantum Hall effect in a bulk antiferromagnet $EuMnBi_2$ with magnetically confined two-dimensional Dirac fermions. *Science Advances* **2** 1 e1501117 (2016).
- [32] Stoyko, S. S.; Mar, A. Ternary rare-earth zinc arsenides $REZn_{1-x}As_2$ ($RE = La-Nd, Sm$). *Journal of Solid State Chemistry* **184** 9 2360-2367 (2011).
- [33] Rutzinger, D.; Bartsch, C.; Doerr, M.; Rosner, H.; Neu, V.; Doert, Th.; Ruck, M. Lattice distortions in layered type arsenides $LnTAs_2$ ($Ln=La-Nd, Sm, Gd, Tb; T=Ag, Au$): Crystal structures, electronic and magnetic properties. *Journal of Solid State Chemistry* **183** 3 510-520 (2010).
- [34] Supporting Information available online at [http://www. \(...\)](http://www. (...))
- [35] Nientiedt, A. T.; Jeitshko, W. The Praseodymium Zinc Arsenide $Pr_3Zn_2As_6$: Crystallizing with a Vacancy Variant of the $HfCuSi_2$ Type Structure. *J. Solid State Chem.* **142** 266 (1999).
- [36] Klintberg, L. E.; Goh, S. K.; Alireza, P. L.; Saines, P. J.; Tompsett, D. A.; Logg, P. W.; Yang, J.; Chen, B.; Yoshimura, K.; Grosche, F. M. Pressure- and Composition-Induced Structural Quantum Phase Transition in the Cubic Superconductor $(Sr, Ca)_3Ir_4Sn_{13}$. *Phys. Rev. Lett.* **109** 237008 (2012).
- [37] Israel, C.; Bittar, E. M.; Agüero, O. E.; Urbano, R. R.; Rettori, C.; Torriani, I.; Pagliuso, P. G.; Moreno, N. O.; Thompson, J. D.; Hundley, M. F.; Sarrao, J. L.; Borges, H. A. Crystal structure and low-temperature physical properties of $R_3M_4Sn_{13}$ ($R = Ce, La; M = Ir, Co$) intermetallics. *Physica B* **251** 359-361 (2005).
- [38] Lue, C. S.; Liu, H. F.; Hsu, S.-L.; Chu, M. W.; Liao, H. Y.; Kuo, Y. K. Observation of a possible charge-density-wave transition in cubic $Ce_3Co_4Sn_{13}$. *Physical Review B* **85** 205120 (2012).
- [39] Collave, J. R.; Borges, H. A.; Ramos, S. M.; Hering, E. N.; Fontes, M. B.; Baggio-Saitovitch, E.; Mendonça-Ferreira, L.; Bittar, E. M.; Pagliuso, P. G. Heavy fermion $Ce_3Co_4Sn_{13}$ compound under pressure. *Journal of Applied Physics* **117** 17E307 (2015).
- [40] Mendonça-Ferreira, L.; Carneiro, F. B.; Fontes, M. B.; Baggio-Saitovitch, E.; Veiga, L. S. I.; Mardegan, J. R. L.; Stremper, J.; Piva, M. M.; Pagliuso, P. G.; dos Reis, R. D.; Bittar, E. M. Pressure effects on the structural and superconducting transitions in $La_3Co_4Sn_{13}$. *Journal of Alloys and Compounds* **773** 34-39 (2019).
- [41] Kwei, G. H.; Lawrence, J. M.; Canfield, P. C.; Beyersmann, W. P.; Thompson, J. D.; Fisk, Z.; Lawson, A. C.; Goldstone, J. A. Thermal expansion of $Ce_3Bi_4Pt_3$ at am-

bient and high pressures. Phys. Rev. B **46** 8067 (1992).

Supporting information for: Robust narrow-gap semiconducting behavior in square-net $\text{La}_3\text{Cd}_2\text{As}_6$

Mario M. Piva,^{1,2,3,*} Marein C. Rahn,^{1,4} Sean M. Thomas,¹ Brian L. Scott,¹ Pascoal G. Pagliuso,² Joe D. Thompson,¹ Leslie M. Schoop,⁵ Filip Ronning,¹ and Priscila F. S. Rosa¹

¹*Los Alamos National Laboratory, Los Alamos, New Mexico 87545, USA*

²*Instituto de Física “Gleb Wataghin”, UNICAMP, 13083-859, Campinas, SP, Brazil*

³*Max Planck Institute for Chemical Physics of Solids, Nöthnitzer Str. 40, D-01187 Dresden, Germany*

⁴*Institute for Solid State and Materials Physics, Technical University of Dresden, 01062 Dresden, Germany*

⁵*Department of Chemistry, Princeton University, Princeton, NJ, 08544, USA*

(Dated: May 12, 2021)

I. ANALYSIS OF X-RAY DIFFRACTION DATA

By considering the structure factor of the $3 \times 1 \times 3$ tetragonal supercell discussed in the manuscript, it can be shown analytically that the $C/2m$ structure is the only vacancy pattern compatible with the superstructure reflection pattern observed in the $(h, 0, l)$ plane. The space group describing this atomic arrangement was identified using the FINDSYM algorithm of the ISOTROPY software suite^{1,2}. A more quantitative analysis of the observed intensities was achieved as follows.

The Rigaku CrysAlisPro package was used to search the detector images for Bragg peaks and index them³. For both compounds ($\text{La}_3\text{Cd}_2\text{As}_6$ and $\text{Ce}_3\text{Cd}_2\text{As}_6$), a close to complete ($> 98\%$) indexation of all observed peaks was achieved in the $C2/m$ cell ($a \sim 21.6$, $b \sim 4.1$, $c \sim 12.2$, $\beta \sim 100.8^\circ$). Two (La) and four (Ce) crystallographic twins were taken into account, respectively. The intensities were integrated, and reprocessed for twinning, as implemented in CrysAlisPro.

The structures were solved using the Superflip charge flipping⁴ and EDMA⁵ Fourier peak search approach as implemented in Jana2006^{6,7}. The algorithm reproducibly converged to the atomic arrangement presented in the manuscript. The position parameters of the $4i$ Wyckoff positions in $C2/m$ were then refined using Jana2006 and are summarized below in Tables III and IV. The quality of the refinement is limited by the strong overlap of weak superstructure intensities that have to be assigned to multiple twins.

II. PSEUDO-TETRAGONAL STRUCTURES

Tables I and II show the refinement results of $\text{LaCd}_{2/3}\text{As}_2$ and $\text{CeCd}_{2/3}\text{As}_2$ XRD datasets when treated as non-stoichiometric tetragonal compounds (with $\sim 33\%$ disordered Cd vacancies), i.e. ignoring any superstructure reflections. Given that we have demonstrated the breaking of the 4-fold symmetry in these crystals, Tables I and II should not be perceived as correct crystallographic data but merely represent *hypothetical* compounds. The purpose of these refinements is to estimate the positions of La/Ce and As2 ions along the z -axis. We use this information to infer the atomic displacements dx and dz (cf. Tables III and IV) relative to these (*hypothetical*) tetragonal compounds. The comparison of goodness-of-fit and residual (R) values between the $I4/mmm$ and $C2/m$ refinements also provides some guidance to the level of improvement of the refinement quality by taking into account the true symmetry of the materials. These parameters are defined as

$$R(F) = \frac{\sum ||F_o| - |F_c||}{\sum |F_o|}, \quad \text{for } F_o^2 > 2\sigma(F_o^2)$$

$$R_w(F_o^2) = \left[\frac{\sum [w(F_o^2 - F_c^2)^2]}{\sum w(F_o^2)^2} \right]^{1/2},$$

where F_o and F_c are the observed and calculated structure factors.

LaCd _{2/3} As ₂						CeCd _{2/3} As ₂							
Formula mass (g/mol)	364.1					Formula mass (g/mol)	365.3						
Temperature (K)	293					Temperature (K)	293						
Crystal System	tetragonal					Crystal System	tetragonal						
Space Group	$I4/mmm$ (#139)					Space Group	$I4/mmm$ (#139)						
f.u./cell (Z)	4					f.u./cell (Z)	4						
a (Å)	4.1030(6)					a (Å)	4.0709(6)						
b (Å)	4.1030(5)					b (Å)	4.0709(4)						
c (Å)	21.356(3)					c (Å)	21.227(3)						
α (°)	90.000(11)					α (°)	90.000(9)						
β (°)	90.000(12)					β (°)	90.000(11)						
γ (°)	90.000(12)					γ (°)	90.000(10)						
V (Å ³)	359.52(9)					V (Å ³)	351.78(8)						
ρ_{calcd} (g/cm ³)	6.7261					ρ_{calcd} (g/cm ³)	6.8971						
F (000)	614					F (000)	624						
2θ (°)	1.91 - 29.39					2θ (°)	1.92 - 29.00						
Crystal Size (μm^3)	$25 \times 20 \times 15$					Crystal Size (μm^3)	$25 \times 20 \times 15$						
Radiation	Mo K α					Radiation	Mo K α						
Wavelength (Å)	0.71					Wavelength (Å)	0.71						
μ (mm ⁻¹)	33.723					μ (mm ⁻¹)	35.261						
Number of reflections	177					Number of reflections	174						
Parameters	9					Parameters	8						
Structure factor coefficient	$ F $					Structure factor coefficient	$ F $						
Goodness of fit	5.30					Goodness of fit	4.94						
$R(F)$ (%)	10.33					$R(F)$ (%)	9.60						
$R_w(F_o^2)$ (%)	12.27					$R_w(F_o^2)$ (%)	10.53						
atomic positions						atomic positions							
ion	Wyck.	x	y	z	U_{iso}	occ. (%)	ion	Wyck.	x	y	z	U_{ani}	occ. (%)
La	4e	0	0	0.1094(1)	0.009(2)	100	Ce	4e	0	0	0.1087(1)	0.004(1)	100
Cd	4d	0	1/2	1/4	0.030(3)	63(2)	Cd	4d	0	1/2	1/4	0.027(3)	62(2)
As1	4c	0	1/2	0	0.022(2)	100	As1	4c	0	1/2	0	0.013(1)	100
As2	4e	0	0	0.3351(3)	0.011(2)	100	As2	4e	0	0	0.3365(2)	0.006(1)	100

TABLE I. Structural refinement of $\text{LaCd}_{2/3}\text{As}_2$ as a *hypothetical* tetragonal compound with Cd vacancies.

TABLE II. Structural refinement of $\text{CeCd}_{2/3}\text{As}_2$ as a *hypothetical* tetragonal compound with Cd vacancies.

III. REFINED MONOCLINIC ($C2/m$) STRUCTURES

Tables III and IV summarize the refinements of the same XRD datasets (as in Tables I and II) in the monoclinic $C2/m$ cell. This is the correct description, corresponding to stoichiometric “326” compounds. Aside from refined atomic position data, we list the resulting deviations dx and dz in (Å units) from the nominal atomic positions in the respective tetragonal cells, as inferred from Tables I and II. Deviations larger than 0.1 Å are highlighted in red font. The transformation from the tetragonal to monoclinic atomic parameters is stated in Table II of the manuscript.

La₃Cd₂As₆								Ce₃Cd₂As₆							
Formula mass (g/mol)				1091.1				Formula mass (g/mol)				1094.7			
Temperature (K)				293				Temperature (K)				293			
Crystal System				monoclinic				Crystal System				monoclinic			
Space Group				$C2/m$ (#12)				Space Group				$C2/m$ (#12)			
f.u./cell (Z)				4				f.u./cell (Z)				4			
a (Å)				21.732(8)				a (Å)				21.621(9)			
b (Å)				4.0928(15)				b (Å)				4.0634(14)			
c (Å)				12.323(3)				c (Å)				12.224(2)			
α (°)				90.00(3)				α (°)				90.00(2)			
β (°)				100.92(3)				β (°)				100.84(2)			
γ (°)				90.00(3)				γ (°)				90.00(3)			
V (Å ³)				1076.2(6)				V (Å ³)				1054.8(6)			
ρ_{calcd} (g/cm ³)				6.7338				ρ_{calcd} (g/cm ³)				6.8937			
F (000)				1860				F (000)				1872			
2θ (°)				1.91 - 29.39				2θ (°)				1.70 - 29.53			
Crystal Size (μm^3)				$25 \times 20 \times 15$				Crystal Size (μm^3)				$25 \times 20 \times 15$			
Radiation				Mo K_{α}				Radiation				Mo K_{α}			
Wavelength (Å)				0.71				Wavelength (Å)				0.71			
μ (mm ⁻¹)				33.778				μ (mm ⁻¹)				35.261			
Number of reflections				2085				Number of reflections				4258			
Parameters				33				Parameters				42			
Structure factor coefficient				$ F $				Structure factor coefficient				$ F $			
Goodness of fit				2.30				Goodness of fit				1.70			
$R(F)$ (%)				8.51				$R(F)$ (%)				6.71			
$R_w(F_o^2)$ (%)				9.87				$R_w(F_o^2)$ (%)				8.54			

La ₃ Cd ₂ As ₆								Ce ₃ Cd ₂ As ₆							
atomic positions				deviations (Å)				atomic positions				deviations (Å)			
ion	W.	x	y	z	dx	dz	U	ion	W.	x	y	z	dx	dz	U
La1	4i	0.10945(15)	0	0.0374(7)	±0	+0.020	0.0040(10)	Ce1	4i	0.10901(12)	0	0.0399(3)	+0.007	+0.045	0.0067(9)
La2	4i	0.10965(15)	0	0.7021(8)	+0.007	-0.022	0.0040(10)	Ce2	4i	0.10917(12)	0	0.7046(3)	+0.010	+0.021	0.0065(9)
La3	4i	0.10897(16)	0	0.3665(7)	-0.009	-0.071	0.0040(10)	Ce3	4i	0.10831(12)	0	0.3686(3)	-0.008	-0.012	0.0056(8)
Cd1	4i	0.25135(20)	0	0.8947(8)	+0.029	-0.271	0.0103(7)	Cd1	4i	0.2516(2)	0	0.8949(5)	+0.035	-0.266	0.0124(5)
Cd2	4i	0.25130(19)	0	0.6016(8)	+0.028	+0.225	0.0103(7)	Cd2	4i	0.2516(2)	0	0.6024(5)	+0.035	+0.233	0.0124(5)
As1	4i	0.3328(3)	0	0.1115(14)	-0.050	-0.003	0.0101(6)	As1	4i	0.3343(2)	0	0.1130(6)	-0.048	+0.010	0.008(1)
As2	4i	0.3399(3)	0	0.7787(14)	+0.104	+0.004	0.0101(6)	As2	4i	0.34176(19)	0	0.7814(6)	+0.114	+0.031	0.0052(14)
As3	4i	0.3332(3)	0	0.4442(14)	-0.041	-0.010	0.0101(6)	As3	4i	0.3340(2)	0	0.4458(6)	-0.054	+0.037	0.008(1)
As4	2b	0	1/2	0	—	—	0.0101(6)	As4	2b	0	1/2	0	—	—	0.08(1)
As5	4i	0.0005(4)	0	0.1770(5)	+0.011	+0.127	0.0101(6)	As5	4i	0.9990(3)	0	0.1773(3)	-0.022	+0.130	0.008(1)
As6	4i	0.5013(5)	0	0.3488(5)	+0.028	+0.191	0.0101(6)	As6	4i	0.4992(4)	0	0.3490(4)	+0.017	+0.192	0.008(1)
As7	2c	0	0	1/2	—	—	0.0101(6)	As7	2c	0	0	1/2	—	—	0.008(1)

TABLE III. Structural refinement of La₃Cd₂As₆.TABLE IV. Structural refinement of Ce₃Cd₂As₆.

REFERENCES

- [1] Stokes, H. T.; Hatch, D. M. FINDSYM: program for identifying the space-group symmetry of a crystal, *Journal of Applied Crystallography* **38** 237 (2005).
- [2] Stokes, H. T.; Hatch, D. M.; Campbell, B. J. Findsymb, isotropy software suite, iso.byu.edu.
- [3] Agilent Technologies, (2013), CrysAlisPro Software system, Agilent Technologies UK Ltd, Oxford, UK.
- [4] Oszlányi, G.; Süto, A. *Ab initio* structure solution by charge flipping. *Acta Crystallographica Section A* **60** 134 (2004).
- [5] Palatinus, L.; Prathapa, S. J.; van Smaalen, S. EDMA: a computer program for topological analysis of discrete electron densities. *Journal of Applied Crystallography* **45** 575 (2012).
- [6] Petříček, V.; Dušek, M.; Palatinus, L. Crystallographic computing system jana2006: General features. *Zeitschrift für Kristallographie - Crystalline Materials* **229** 345 (2014).
- [7] Petříček, V.; Dušek, M.; Plíšil, J. Crystallographic computing system jana2006: solution and refinement of twinned structures. *Kristallographie - Crystalline Materials* **231** 582 (2016).